Postprint of: Adibimanesh B., Ayani M. B., Khozeymeh-Nezhad H., Polesek-Karczewska S., Applying response surface method to optimize the performance of a divergent-chimney solar power plant, Sustainable Energy Technologies and Assessments, Vol. 48 (2021), 101593, DOI: 10.1016/j.seta.2021.101593

Applying Response Surface Method to optimize the performance of a Divergent-Chimney Solar Power Plant

Behrouz Adibimanesh[a], Mohammad Bagher Ayani[b*], Hojjat Khozeymeh-Nezhad[b] and Sylwia Polesek-Karczewska[c]

[a] Doctoral School of Gdansk University of Technology, Narutowicza 11/12, 80-233, Gdańsk, Poland
[b] Department of Mechanical Engineering, Faculty of Engineering, Ferdowsi University of Mashhad, Mashhad, Iran
[c] Institute of Fluid Flow Machinery, Polish Academy of Sciences, Fiszera 14, 80-231, Gdańsk, Poland

Abstract

One of the effective tools to generate electricity from solar energy is Divergent-chimney solar power plant (DSPP). Divergent and cylindrical chimneys of solar power plants have different performances considering turbine pressure drop ratio (ft). For the first time, the divergent angle (*DA*) and solar radiation (*SR*) interaction effects on ft_{opt} are discussed through applying the Computational Fluid Dynamics (CFD) and Response Surface Method (RSM). FLUENT software is employed to perform 2D axisymmetric numerical stimulation for the Manzanares prototype. The *DA*, *SR*, and ft with ranges of 0°-3°, 200-800 W/m^2, and 0.2-0.9 are considered, respectively, in the RSM optimization. The outcomes denote that the amount of ft_{opt}varies from 0.71 to 0.89 continuously, and it is related inversely to the *DA* and directly to the *SR*. The maximum efficiency (η_{max}) is obtained at ft_{opt}, for different *SR*s and *DA*s. It is concluded that the η_{max} is enhanced from 0.42% to 0.50%, achieved by increasing the *DA* and *SR* values. Furthermore, the quadratic correlation of the ft_{opt} and η_{max} in terms of *DA* and *SR* parameters are provided. Therefore, the consequences of this research would be a suitable resource for designing optimum turbines for the DSPPs.

Keywords: Turbine pressure drop, Divergent chimney, Solar chimney power plant, Optimal ratio, Maximum efficiency

Nomenclature

$\dot{E}_{in}$	Total input energy rate		
C_p	specific heat capacity [J/kg K]	*SR*	solar radiation
H	height [m]	Δp_{loss}	System pressure drop
$\dot{W}_t$	the output power of turbine [W]	Δp_{total}	Total pressure potential
p	static pressure [Pa]	Δp_{turb}	Turbine pressure drop
Ra	Rayleigh number		
		Subscript	
		a	air
Acronyms		ch	chimney
CCD	central composite design	f	fluid
CFD	computational fluid dynamics	in	inlet
CSPP	cylindrical-chimney solar power plant	max	maximum
DA	the divergent angle of the chimney	opt	optimum
DSPP	divergent-chimney solar power plant	out	outlet
SCPP	Solar chimney power plant	*Greek symbols*	
FCCCD	face centered central composite design	β	volumetric thermal expansion coefficient [1/K]
ft	turbine pressure drop ratio	η	efficiency
RSM	response surface method	η_{max}	efficiency at optimal turbine pressure
Adeq	adequate precision	ρ	density [kg/m^3] drop

1. Introduction

Harmful effects of fossil fuel overuse, e.g., air pollution and global warming, have stimulated the human tendency to use environment-friendly renewable energy resources. The transformation of solar radiation to electrical energy is conducted via a solar chimney power plant (SCPP). The plant consists of three principal parts: Wind turbine, Chimney, and Collector. The air temperature increases while passing through the collector due to the sun's radiant energy absorption. Therefore, since there is a difference between the density of ambient air and the air in the collector, the air density is reduced and the buoyant force is created which pushes the air out of the chimney. The turbine converts the air kinetic energy to a rotary motion [1–3].

The idea of electricity generation with SCPP was first introduced by the initial prototype of SCPP in 1970-Manzanares [1]. Early studies showed that small-scale SCPP had lower efficiency (η) in comparison with large-scale SCPPs [4,5]. There has been considerable investigations on the critical role of chimney height and collector radius in generating electrical power of SCPP [6–8]. The research studies were not limited to the size of the SCPP. The output power is enhanced by altering the chimney shape from cylindrical to divergent, i.e., the higher the chimney outlet diameter, the less kinetic energy and the more power plant efficiency achieved [9,10]. Therefore, optimizing the divergent angle of the chimney (*DA*) or the area fraction of the chimney inlet to the chimney outlet has been essential to produce more output power. The schematic view of the Divergent SCPP is represented in Fig.1.

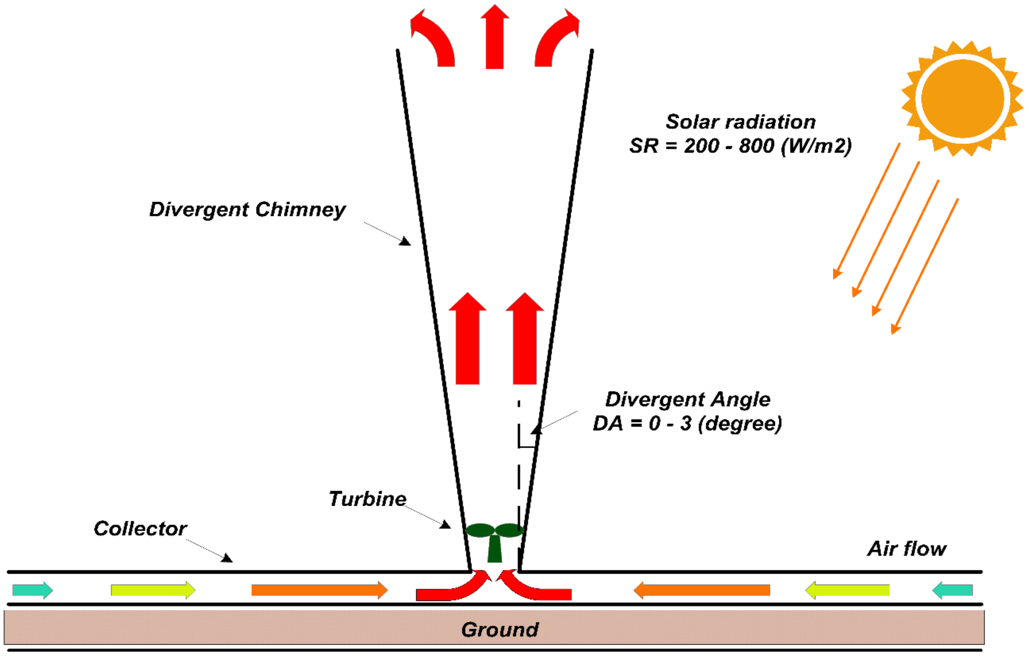

Fig. 1 Divergent solar chimney power plant (schematic view)

Higher static pressure and mass flow rate are caused by increasing the slopping collector roof and *DA* compared to the cylindrical-chimney solar power plant (CSPP). In contrast, the output power was enhanced significantly, as shown by numerical simulation [11,12]. The performance improvement of SCPP was studied by employing a 3D numerical study, applying various geometric variables; chimney diameter, collector inlet opening, and *DA* [13]. It was shown by an experimental study on small dimensions of DSPP taking into account the ambient conditions, that the production capacity of the power plant was increased by 4-5 times comparing with CSPP [14]. The optimum value of *DA* and area ratio were obtained in which the power output was maximized. At the same time, temperature differences at environment and chimney inlet were decreased by the diffuser stall occurring and increase of the mass flow [15]. Zhou and Xu [16] investigated the effect of backflow on divergent-chimney solar power plant (DSPP) through 3D numerical simulation of the Manzanares prototype. They showed that the backflow area became larger with an increase of *DA*. Furthermore, it was shown that a more negligible difference in the outlet and inlet temperature of the chimney caused less buoyancy and volume flow rate. In a recent study, the novel chimney shape was designed to deal with the boundary layer separation phenomenon [17]. Technologically speaking, building DSPP on a large scale and erecting a tall chimney with a divergent angle is challenging and requires advanced construction techniques. However, it can be built today with civil engineering development. Designing the DSPP in optimal dimension was suggested due to the high initial investment costs [18].

Additionally, several researches investigated the turbine design to enhance the efficiency (η) of SCPP. The fluid flow energy can be transformed into mechanical energy using the aerodynamic force from the rotor blades. The fluid flow on the blades rotates main shaft and generator to produce electric power. The turbine's aerodynamic design and proper operation are determined by Turbine pressure drop (Δp_{turb})[19]. Thus, the turbine pressure drop ratio (ft) was investigated in several studies. In a pioneer work [20], the optimal value of the ft was calculated ($ft_{opt} = 2/3$). This value was corrected due to the constant temperature rise assumption in a collector and a new value of around 0.9 was suggested [4]. Backström and Fluri [21] assumed a correlation of volumetric flow rate and total pressure potential, wherein maximum fluid power occurred in larger values of Δp_{turb} as well as smaller flow rate than the corresponding values given by constant pressure potential assumption. Nizetic and Klarin [22] conducted an analytical approach to find the ft_{opt}, which was approximately equal to the values reported in [4]. The effect of Δp_{turb} on the output power and the wasted energy for different solar radiations (*SR*s) is investigated by 2D numerical study [23]. Aligholami et al. [24] investigated the effect of turbine pressure jump and geometrical factors on the performance of SCPP simultaneously by implying exergy and energy analysis. Li and Guo [25] examined the impact of *SR* and collector radius on ft_{opt} in solar chimney-aided dry cooling systems. Guo et al. [26] obtained the ft_{opt} of about 0.9 applying a 3D numerical model considering the power-law relationship for output velocity and temperature rise. It was shown that the results achieved in real turbine model were comparable with those in the fan model [27]. In addition, Guo et al. [28] calculated the ft_{opt} for different *SR*s and ambient temperatures in the two modes of a circular and square collector. The performance of the turbine was dramatically improved by using new lifting design method and the variation of ft_{opt} was reported 0.9 to 0.92 [29].

Although it was shown that the divergent chimney and optimal operation of the turbine enhance the performance of SCPP separately, this study uniquely aims to reach the highest efficiency considering both terms simultaneously. Scrutinization of similar literature reveals that there have not been any studies on an investigation of ft_{opt} by considering the divergent angle of the chimney (*DA*) and solar radiation (*SR*). As a result, it is essential to investigate the values of ft for accommodating a variation in practical operation. In this article, the Computational Fluid Dynamics (CFD) is integrated with the Response Surface Method (RSM) to propose an effective technique (CFD-RSM) for detailed analyses of the DSPP.

2. Material and methods

2.1 Mathematical model

Equations for fluid flow through the 2D axisymmetric SCPP are continuity, momentum, and energy equation. For example, the mass continuity at the steady-state is given by:

$$\frac{\partial(\rho u)}{\partial z} + \frac{1}{r}\frac{\partial(r\rho v)}{\partial r} = 0 \qquad (1)$$

Where v and u are velocity components along r and z direction and ρ is density. The density varies based on Boussinesq approximation is given by:

$$\rho = \rho_0\big(1 - \beta(\mathrm{T} - T_0)\big) \qquad (2)$$

wherein ρ_0 is the reference ambient density, T_0 is the reference temperature, β is the coefficient of thermal expansion. In natural convection, the Ra number is evaluated to distinguish the flow regime, which is defined by [23]:

$$Ra = \frac{g\beta\Delta T L^3}{\alpha v} \qquad (3)$$

The average height of collector and the thermal diffusivity are denoted by L and α, respectively. Air temperature rises at the collector (ΔT) is obtained through conservation of energy at the collector as:

$$\Delta T = \frac{\dot{Q}_{in}}{\rho \dot{V} c_p} \tag{4}$$

in which $\dot{V}$ and c_p are volume flow rate and specific heat capacity of the system flowing through a chimney outlet, respectively. $\dot{Q}_{in}$ denotes the net rate of thermal energy from the ground and collector to the air. An analysis conducted throughout the collector and chimney resulted in $Ra > 10^{10}$ [23], thus the momentum conservation equations of steady turbulent buoyant flow are:

$$\frac{\partial}{\partial z}(\rho u u) + \frac{1}{r}\frac{\partial}{\partial r}(r\rho v u) = \frac{\partial}{\partial z}\left((\mu+\mu_t)\frac{\partial u}{\partial z}\right) + \frac{1}{r}(\frac{\partial}{\partial r}(\mu+\mu_t) r\frac{\partial u}{\partial r} + \rho g \beta (T - T_0) + \frac{\partial}{\partial z}\left((\mu+\mu_t)\frac{\partial u}{\partial z}\right) + \frac{1}{r}\frac{\partial}{\partial r}\left((\mu+\mu_t) r\frac{\partial v}{\partial z}\right) \tag{5}$$

$$\frac{\partial}{\partial z}(\rho u v) + \frac{1}{r}\frac{\partial}{\partial r}(r\rho v v) = \frac{\partial}{\partial z}\left((\mu+\mu_t)\frac{\partial v}{\partial z}\right) + \frac{1}{r}(\frac{\partial}{\partial r}(\mu+\mu_t) r\frac{\partial v}{\partial r} - \frac{\partial p}{\partial r} + \frac{\partial}{\partial z}\left((\mu+\mu_t)\frac{\partial u}{\partial r}\right) + \frac{1}{r}\frac{\partial}{\partial r}\left((\mu+\mu_t) r\frac{\partial v}{\partial r}\right) - \frac{2(\mu+\mu_t)v}{r^2} \tag{6}$$

The k-ε turbulent model is applied in this study, including two equations; turbulent eddy dissipation (ε) and turbulent kinetic energy (K):

$$\frac{\partial}{\partial z}(u\varepsilon) + \frac{1}{r}\frac{\partial}{\partial r}(r v \varepsilon) = \frac{1}{\rho}\frac{\partial}{\partial z}\left(\left(\mu + \frac{\mu_t}{\sigma_\varepsilon}\right)\frac{\partial \varepsilon}{\partial z}\right) + \frac{1}{\rho r}\frac{\partial}{\partial r}\left(\left(\mu + \frac{\mu_t}{\sigma_\varepsilon}\right) r \frac{\partial \varepsilon}{\partial r}\right) + \frac{\varepsilon}{k}(C_1 G_k - C_2 \varepsilon) \tag{7}$$

$$\frac{\partial}{\partial z}(u k) + \frac{1}{r}\frac{\partial}{\partial r}(r v k) = \frac{1}{\rho}\frac{\partial}{\partial z}\left(\left(\mu + \frac{\mu_t}{\sigma_k}\right)\frac{\partial k}{\partial z}\right) + \frac{1}{\rho r}\frac{\partial}{\partial r}\left(\left(\mu + \frac{\mu_t}{\sigma_k}\right) r \frac{\partial k}{\partial r}\right) + G_k - \varepsilon \tag{8}$$

Average velocity gradients produced turbulent kinetic energy, which is defined by G_k. $C_1 = 1.44$ and $C_2 = 1.92$ are the turbulent model constants. The corresponding turbulent Prandtl numbers; ε, k, and T are utilized for σ_ε, σ_k, and σ_T. An energy equation in axisymmetric configuration is expressed as:

$$\frac{\partial}{\partial z}(uT) + \frac{1}{r}\frac{\partial}{\partial r}(rvT) = \frac{1}{\rho}\frac{\partial}{\partial z}\left(\left(\frac{\mu}{Pr} + \frac{\mu_t}{\sigma_T}\right)\frac{\partial T}{\partial z}\right) + \frac{1}{\rho r}\frac{\partial}{\partial r}\left(\left(\frac{\mu}{Pr} + \frac{\mu_t}{\sigma_T}\right) r \frac{\partial T}{\partial r}\right) \tag{9}$$

2.2 Theoretical model of ft_{opt} for maximum output power in DSPP and CSPP

One of the main designing parameters to enhance the performance of SCPP is ft. The different effects of ft on the output power in DSPP and CSPP are discussed in the following part. The efficiency (η) of SCPP is calculated by dividing the turbine's output power ($\dot{W}_t$) by the total input energy ($\dot{E}_{in}$) [30,31]:

$$\eta = \frac{\dot{W}_t}{\dot{E}_{in}} \tag{10}$$

where $\dot{E}_{in}$ is obtained by multiplying the solar energy (SR) by the collector area (A_{coll}):

$$\dot{E}_{in} = SR \times A_{coll} \tag{11}$$

The turbine's output power ($\dot{W}_t$) is calculated as follows:

$$\dot{W}_t = \Delta p_{turb}\ \dot{V} \tag{12}$$

where Δp_{turb} represents the turbine pressure drop [23]. The pressure difference between inlet ($P_{in,ch}$) and outlet ($P_{out,ch}$) of a chimney is obtained by integrating the Navier–Stokes equation [15]:

$$P_{in,ch} - P_{out,ch} = \frac{1}{2}\,\rho_f\left({v_{out,ch}}^2 - {v_{in,ch}}^2\right) + \Delta p_{turb} + \Delta p_{loss} + \rho_f gH \tag{13}$$

wherein $v_{out,ch}$ and $v_{in,ch}$ are the velocities at the chimney's outlet and inlet, respectively. The static pressure relationship for ambient air integrated with the Boussinesq approximation for the difference in a fluid density in order to calculate the total pressure potential (Δp_{total}) for DSPP as following:

$$(\rho_0 - \rho_f)gH + \frac{1}{2}\rho_f\left(v_{in,ch}^2 - v_{out,ch}^2\right) = \Delta p_{turb} + \Delta p_{loss} \tag{14}$$

$$\Delta p_{total} = \rho_0\, g\, H\beta\, \Delta T + \frac{1}{2}\rho_f\left(v_{in,ch}^2 - v_{out,ch}^2\right) \tag{15}$$

where ρ_f is air density in the chimney. The expressions for Δp_{turb} is the difference between a total pressure potential and a system pressure drop [21,28]:

$$\Delta p_{turb} = \Delta p_{total} - \Delta p_{loss} \tag{16}$$

Finally, ft is obtained by dividing Δp_{turb} to Δp_{total} [1]:

$$ft = \frac{\Delta p_{turb}}{\Delta p_{total}} \tag{17}$$

The variations of the Δp_{total} and $\Delta p_{loss}$with the volume flow rate in CSPP and DSPP is shown in Fig. 2.

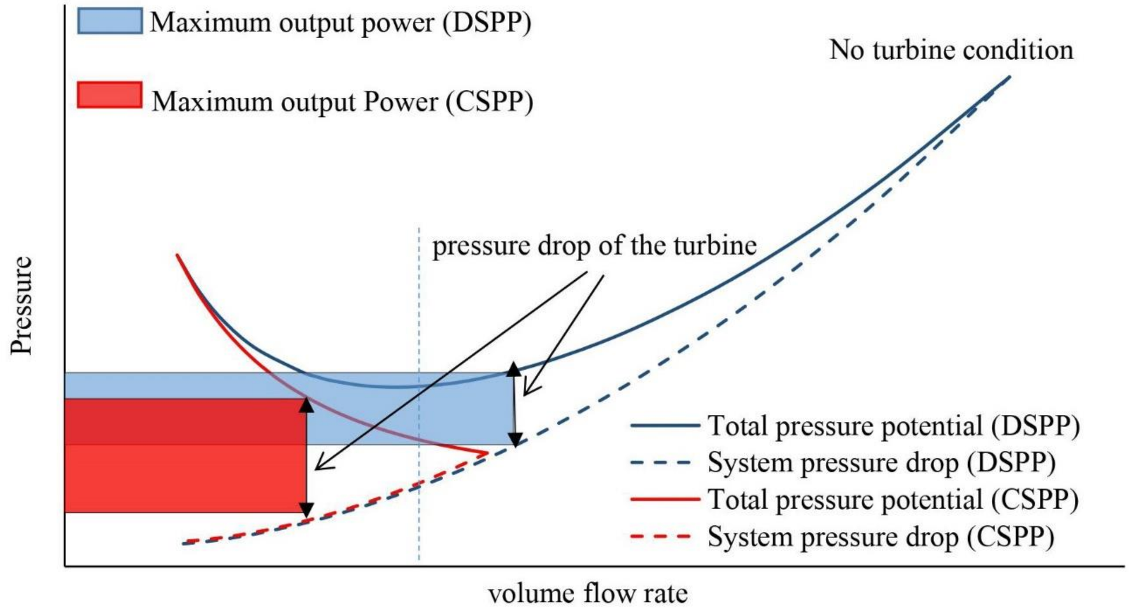

Fig. 2 A schematic diagram of variations of Δp_{total} and Δp_{loss} with the volume flow rate for DSPP and CSPP

According to Eq. (15), Δp_{total} contains two parts, the static pressure recovered and buoyancy. Both terms affect the Δp_{total} value in DSPP case while Δp_{total} varies only by the buoyant term in CSPP since outlet and inlet velocities of the chimney are identical. In CSPP, the temperature rise at the collector decreases with increment of the flow rate; as a result, the Δp_{total} is descending in all ranges of the volume flow rate. Interestingly, DSPP shows similar behavior of Δp_{total} with respect to volume flow rate until it reaches a minimum point. Subsequently, the static pressure recovered becomes dominant term and Δp_{total} starts rising to the no turbine condition. On the other hand, Δp_{loss} increases in both types of the SCPP with the rise of the flow rate according to the power-law relationship [22].

Based on Eq. (12), the maximum power output at two arbitrary volume flow rates is denoted by the domains of red and blue rectangles in Fig. 2. It is worth mentioning that the areas of this rectangle depend upon the volume flow rate. The red and blue rectangles in Fig. 2 represent the maximum output power at optimum turbine pressure drop ratio (ft_{opt}) for CSPP and DSPP, respectively. Considering the different variation of Δp_{total} in CSPP and DSPP, the best performance of DSPP occurred in the higher volume flow rate rather than CSPP. As a result, ft_{opt} is not equal in two different kinds of SCPP.

2.3 Numerical simulation

The SCPP constructed plant in Manzanares contains a collector with a radius of 120 (m) and a chimney with a height of 195 (m) [1]. Hence, to evaluate the efficiency of DSPP, according to the reference case, by considering a constant value for the chimney's height and radius, the chimney's divergence angle is varied from 0° to 3°. Therefore, the main dimensions of the system configuration are presented in Table 1.

Table 1. Main dimensions of the model

Collector			**Chimney**					**Turbine**	
Height (m)	**Inlet radius (m)**	**Outlet radius (m)**	**Height (m)**	**Inlet radius (m)**	**Outlet radius (m)**			**Section area (m^2)**	**Position height (m)**
					***DA*=0°**	***DA*=1.5°**	***DA*=3°**		
1.7	120	13.3	195	5	5	9.8	14.7	70.5	10

ANSYS FLUENT 16 software is utilized to simulate the DSPP as a 2D axisymmetric and steady-state model in this study. The DSPP is divided into two regions containing air and ground, which are considered simultaneously in the provided model by employing the available multi-region tools. The Simple scheme solves the pressure–velocity linked equation for incompressible fluid with the Boussinesq approximation. Turbulent fluid flow was considered due to the ($Ra > 10^{10}$) [32]. The k-ϵ model with standard wall function is applied to simulate the turbulent flow.

Applied boundary conditions are displayed in Table 2. Convection boundary is considered for the thermal transport from the top of the collector to the outer air in which the ambient temperature and convection coefficient are set as $300\ K$ and $8\ \frac{W}{m^2K}$ (considering irradiation of the plant into the atmosphere), respectively [26]. The pressure boundary conditions are assigned to $0\ Pa$ for the outside air by simultaneously considering the system internal and external pressure distributions. Thin film of soil is considered as a thermal source for modeling solar radiation. A fixed temperature of $300\ K$ is used at the below of the ground. The same air velocity is considered for the entrance and exit location of turbine in the SCPP system [23]. Thus, for the turbine modeling purpose, a pressure jump across it was defined.

Table 2. Boundary conditions

place	**Type**	**Value**
Top of the collector	Wall: convection	T_e = 300 K, h = 8 W/ (m^2 K)
Bellow of the ground	Wall: Temperature	300 K
0.1 mm thin film on the ground	Wall: Thermal source	2 – 8 × 10^6 W/m^3
Surface of the chimney	Wall: adiabatic	q_{chim} = 0 W/m^2
Turbine pressure drop	Reverse fan	0 – 400 Pa
Chimney outlet	Pressure outlet	ΔP_{out} = 0, P = P_{atm}
Inlet of the collector	Pressure inlet	P_{in} = P_{atm}, T_0 = 300 K

ICEM 16.0 is utilized to mesh the geometry structurally. Mesh independence analysis was taken out for several grid sizes such that more number of elements are employed in the vicinity of the

bend, glass, ground, and chimney [33,34]. Fig. 3 shows the boundary condition and mesh in the vicinity of the walls and turbine.

The numerical validation is conducted for chimney outlet velocity and temperature rise with an experimental study for a Manzaranes model [1]. Table 3 shows remarkable compatibility (less than 5%) between the obtained experimental results and the present study considering the solar radiation of 1000 W/m^2. Additionally, radial temperature distribution along the mid-plane of the collector is compared with [35] for two solar radiations, as represented in Fig. 4. The maximum error of a present model is less than 2%.

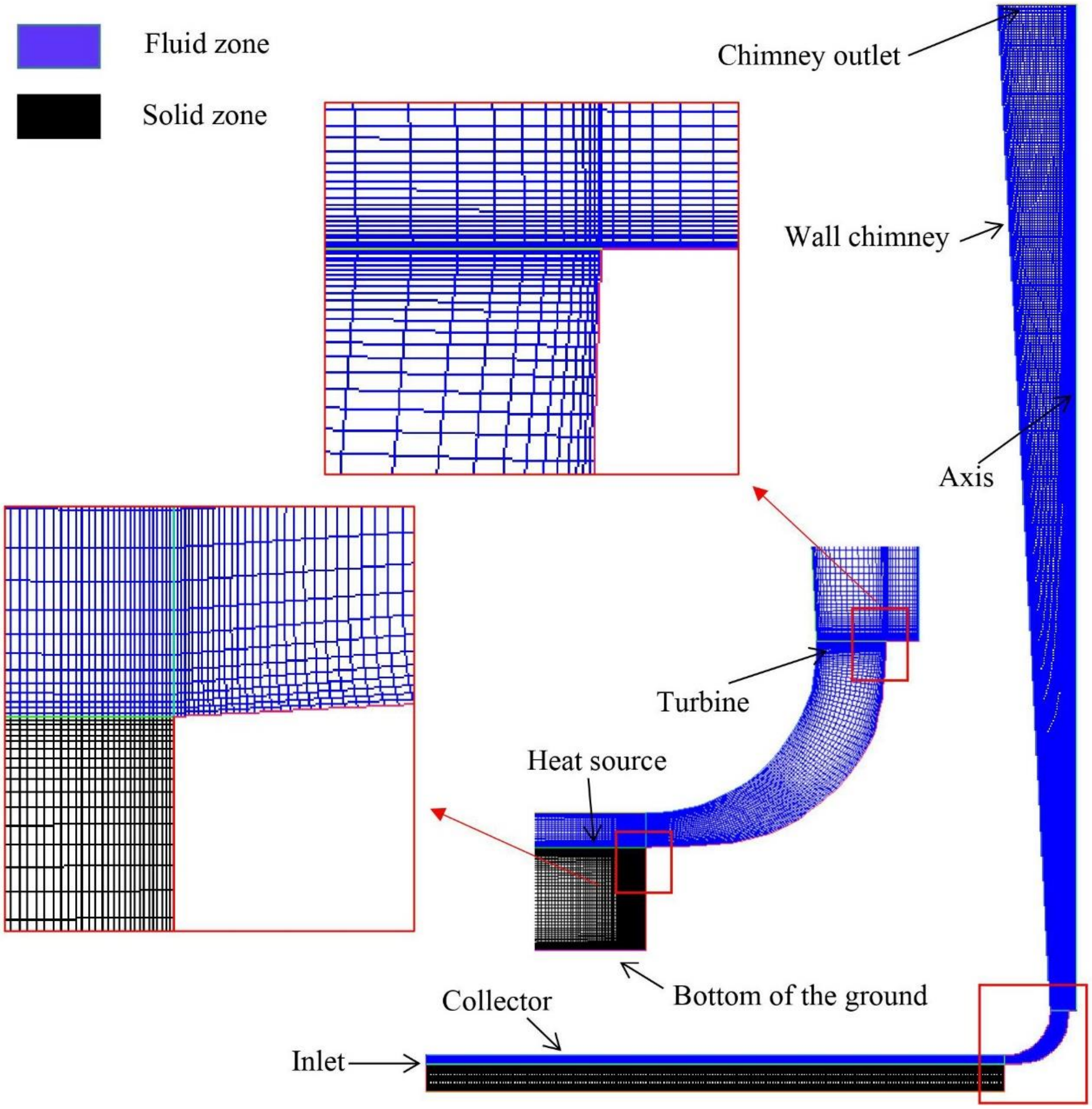

Fig. 3 Mesh and Boundary conditions of the 2D axisymmetric model

Table 3. Experimental data and present study (Comparison)

Results	**Updraft velocity**	**Temperature rise**
Experiment data	15ms^{-1}	20 K
Present study	15.8 ms^{-1}	21 K

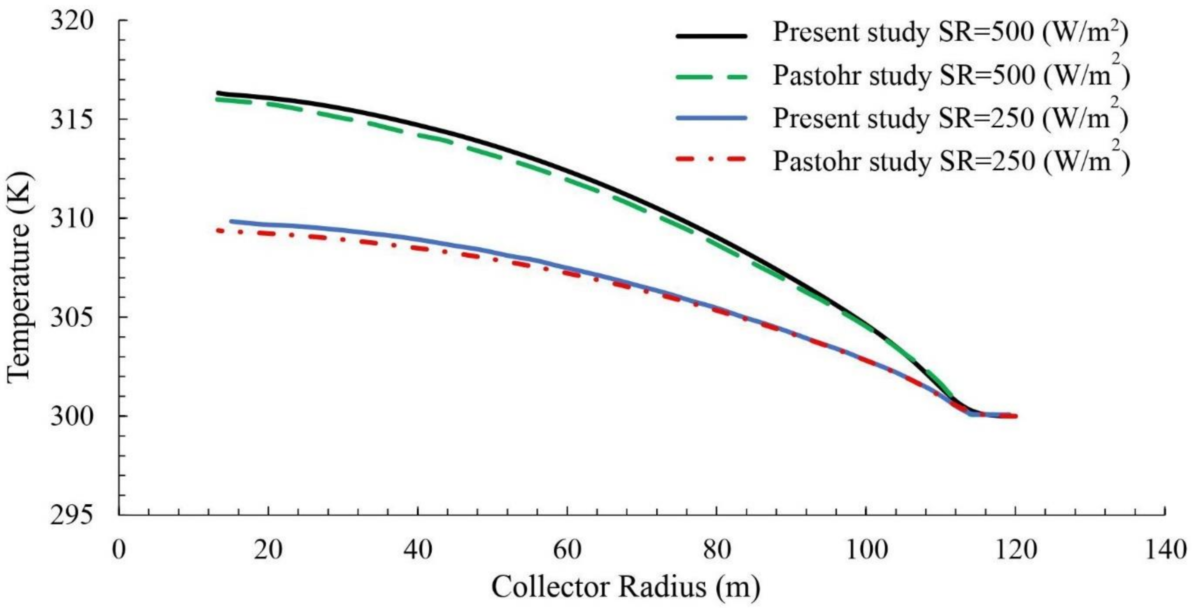

Fig. 4 Comparison of air temperature inside collector between present study and literature

Finally, in order to legitimize an approach utilized in this study, the pressure potential, the mass flow rate, and temperature rise values for three different *DA*s (*SR*=250 W/m^2 under no turbine load) are compared with numerical modeling results in the literature [16]. Specifically, for the DSPP model, this validation is required due to the gap in the experimental study for large geometries, which is applicable in real-life power production. Table 4 depicts the aforementioned quantities for both studies. It should be highlighted that the 7% error is appeared due to the negligible effect of the difference in boundary conditions at the collector of two models.

Table 4. Validation of the present numerical modeling for DSPP with literature

Results	$\boldsymbol{DA = 0°}$			$\boldsymbol{DA = 1.5°}$			$\boldsymbol{DA = 3°}$		
	Pressure potential (Pa)	Temperature rises at the collector (K)	Mass flow rate (kg/s)	Pressure potential (Pa)	Temperature rises at the collector (K)	Mass flow rate (kg/s)	Pressure potential (Pa)	Temperature rises at the collector (K)	Mass flow rate (kg/s)
Zhou study [14]	68.3	11.7	987	265.4	6.1	1886	357.5	5.4	2241
Present study	66.1	11.3	901	288.6	6.6	1734	332.6	5.8	2008

2.4 Response Surface Method

Response Surface Method (RSM) is used to reduce the number of case studies required for analysis, including three schemes; Doehlert, Box-Behnken, and Central Composite Design (CCD), considering a number and range of independent parameters. The well-known three-level CCD scheme called Face Centered Central Composite Design (FCCCD) is chosen. Accordingly, solar radiation (*SR*), divergent angle (*DA*), and turbine pressure drop ratio (ft) with ranges of 200-800 W/m^2, 0°-3°, and 0.2-0.9, are three significant variables of the solar chimney, respectively, and are considered independent variables in this study .The design matrix is presented in Table 5. RSM proposes the sequential set of numerical modeling's to examine the influence of *DA*, ft and *SR* parameters on the responses of η as provided in Table 6. Also, the ft_{opt} and η_{max} are presented in Table 7.

Table 5. Design matrix for the FCCCD

Factors	Levels		
	Low (-1)	**Central (0)**	**High (+1)**
$\boldsymbol{ft}$	0.2	0.55	0.9
$\boldsymbol{DA}$	0	1.5	3
$\boldsymbol{SR}$	200	500	800

Table 6. Actual values of parameters along with its response of η %

Run	Actual values of independent variables		Response ($\boldsymbol{\eta}$ %)		
	$\boldsymbol{DA}$	$\boldsymbol{ft}$	$\boldsymbol{SR = 200}$	$\boldsymbol{SR = 500}$	$\boldsymbol{SR = 800}$
1	0	0.2	0.1210	0.1281	0.1296
2	0	0.55	0.3159	0.3271	0.3323
3	0	0.9	0.4300	0.4538	0.4661
4	1.5	0.2	0.3521	0.3524	0.3526
5	1.5	0.55	0.4600	0.4767	0.4851
6	1.5	0.9	0.4440	0.4681	0.4816
7	3	0.9	0.4447	0.4692	0.4823
8	3	0.2	0.3768	0.3895	0.4033
9	3	0.55	0.4737	0.4916	0.5002

In order to estimate an appropriate response, a second-order polynomial equation is typically suggested via RSM [36]:

$$y = \beta_0 + \beta_1 X_1 + \beta_2 X_2 + \beta_{12} X_1 X_2 + \beta_{11} X_1^2 + \beta_{22} X_2^2 \quad (18)$$

wherein X is an independent variable, β_0 is a constant value and $\beta_{i(=1-2)}$, β_{12}, and $\beta_{ii(=1-2)}$ are linear, mixed, and second terms regression coefficients of the model, respectively. Regression coefficients are calculated, and data analysis is conducted through the Design-Expert software v10.0.3.

Table 7. Actual values of parameters and their responses of ft_{opt} and $\eta_{max}\%$

Run	Actual values of independent variables		Responses	
	DA	SR	ft_{opt}	$\eta_{max}\%$
1	0	800	0.886	0.468
2	0	500	0.879	0.457
3	0	200	0.868	0.438
4	1.5	500	0.746	0.494
5	1.5	200	0.717	0.477
6	1.5	800	0.782	0.503
7	3	200	0.713	0.482
8	3	500	0.72	0.500
9	3	800	0.726	0.509

Through considering the determination coefficients, P-value, and F-value indicators, the Analysis of variance (ANOVA) test [37] is applied to evaluate the validity of the presented model. The more effective model terms are recognized with, the lower P-value and higher F-value. For model improvement purposes, the P-value>0.1 terms are omitted due to negligible effects on the model. Determination coefficients, corresponding to the model fitness, R^2, R^2_{adj}, and R^2_{pred} are the three significant indicators, changing between 0 and 1, in which the 1 shows optimal fitness. Furthermore, the adequate precision (Adeq) is achieved through applying the signal to noise ratio value of above 4 in the regression model. ANOVA results for η is listed in Table 8 with ft_{opt} and η_{max} listed in Table 9.

Table 8. ANOVA results for response of η %

Model terms	**Response**	
	$\boldsymbol{\eta}$ %	
	P-value	F-value
model	<0.0001	70.95
ft	<0.0001	134.13
DA	<0.0001	94.81
$ft \times DA$	0.0003	45.00
ft^2	0.0016	24.65
DA^2	0.0015	25.39

$R^2 = 0.9807$
$R^2_{adj} = 0.9668$
$R^2_{pred} = 0.8115$
Adeq. P. =29.170

Table 9. ANOVA results for response of ft_{opt} and η_{max} %

Model terms	**Responses**			
	$\boldsymbol{ft_{opt}}$		$\boldsymbol{\eta_{max}}$ %	
	P-value	F-value	P-value	F-value
model	<0.0001	169.43	<0.0001	3013.18
SR	0.0029	16.36	<0.0001	3562.97
DA	<0.0001	399.75	<0.0001	8407.69
$SR \times DA$	-	-	0.0333	6.98
SR^2	-	-	<0.0001	154.18
DA^2	<0.0001	92.17	<0.0001	2056.82

$R^2 = 0.9826$	$R^2 = 0.9995$
$R^2_{adj} = 0.9768$	$R^2_{adj} = 0.9992$
$R^2_{pred} = 0.9526$	$R^2_{pred} = 0.9954$
Adeq. P. =35.384	Adeq. P. =181.941

Fig. 5 illustrates the CFD-RSM approach schematically. Different *SR* values with ft and *DA* parameters are input to the numerical model in order to obtain the η. In the first round of the RSM method (Table 6), η is utilized as the response of the independent variables (*DA*, ft) for three different *SR* values, i.e., 200, 500, and 800 W/m^2. The prediction of η as a function of *DA* and ft is taken out in this step. The derivation of that function concerning the ft provides the ft_{opt} and η_{max}. These calculated values are applied as the response of the independent variables (*DA*, *SR*) in the second round of RSM (Table 7). Finally, the η_{max} and ft_{opt} as a function of *DA* and *SR* is predicted.

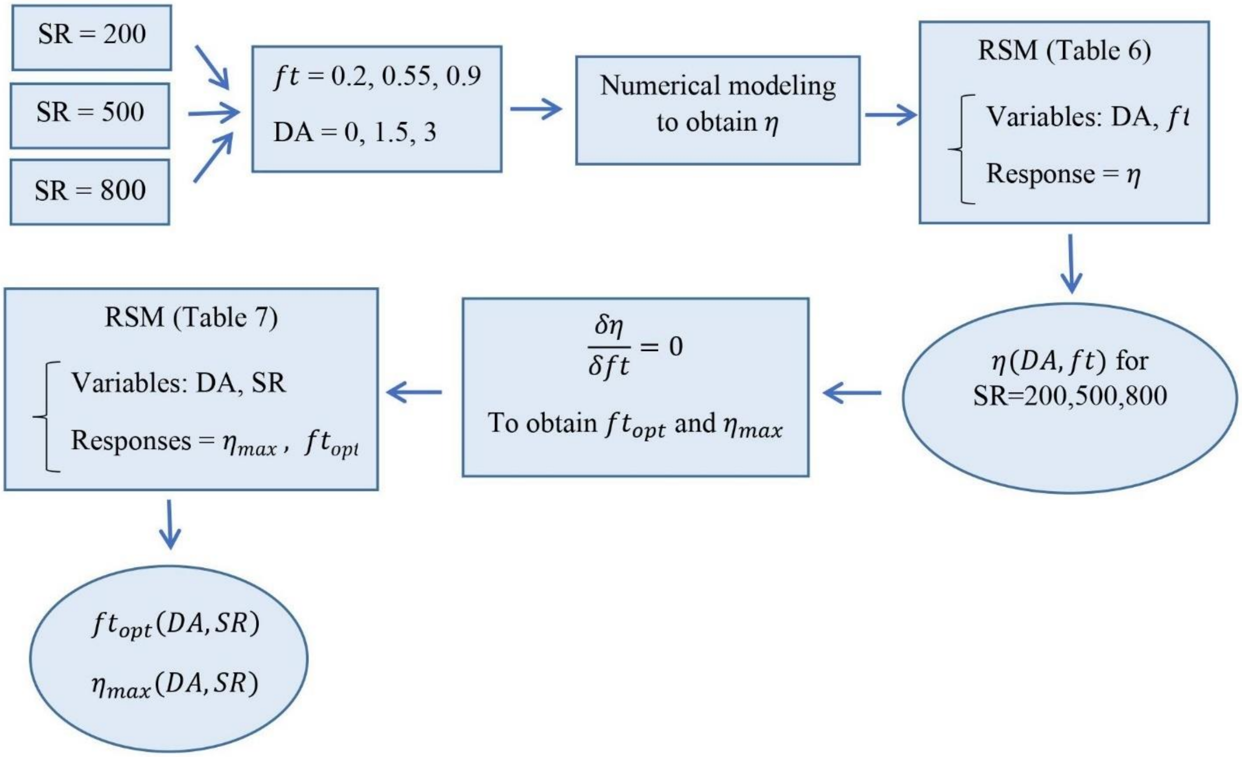

Fig. 5 Schematic view of the CFD-RSM approach

3. Results and discussion

The Manzanares SCPP geometry is utilized through changing *DA* to study the performance of the DSPP model. For this purpose, first, the impacts of the ft and *DA* at different constant *SR*s on the chimney performance are investigated in detail. Next, the ft_{opt} and η_{max} are calculated for different *DA*s and *SR*s. The results given in the initial part of this section are provided only for the *SR*=800 W/m^2.

Fig. 6 shows the velocity distribution at different *DA* and ft. The velocity is increased for all considered *DA*s at the collector. The highest velocity occurred at the chimney inlet because of its minimum cross-sectional area. The velocity remains constant while passing through the turbine because of the pressure-based turbine assumption, i.e., pressure is dropped in the rotor blade with a constant volume flow rate. Therefore, the velocity along the chimney is constant at *DA*=0°. However, it is decreased for other *DA*s due to the invariant cross-sectional area. Also, it is shown that the velocity is related inversely to ft and directly to *DA*.

Fig. 7 represents the impact of *DA* and ft on the temperature distribution. The temperature throughout the two zones, including solid and fluid, is illustrated. It shows that the highest air temperature occurred near the ground. As ft enhances, the gradient of temperature in the solid zone decreased. The heat loss from the bottom of the ground is reduced; thus, the airflow absorbs more heat. Increasing DA leads to an increase in a solid zone temperature gradient, which results in a low temperature of airflow.

The static pressure of the contour is illustrated in Fig. 8. The high values of ft results in high static pressure before entering the turbine while the trend is changed after exiting the turbine. It should be mentioned that the static pressure is reduced by increasing the *DA* at the ft values of 0.2 and 0.55 while it increased at the $ft = 0.9$. In addition, there is a pressure drop at the turbine without any variation of air velocity.

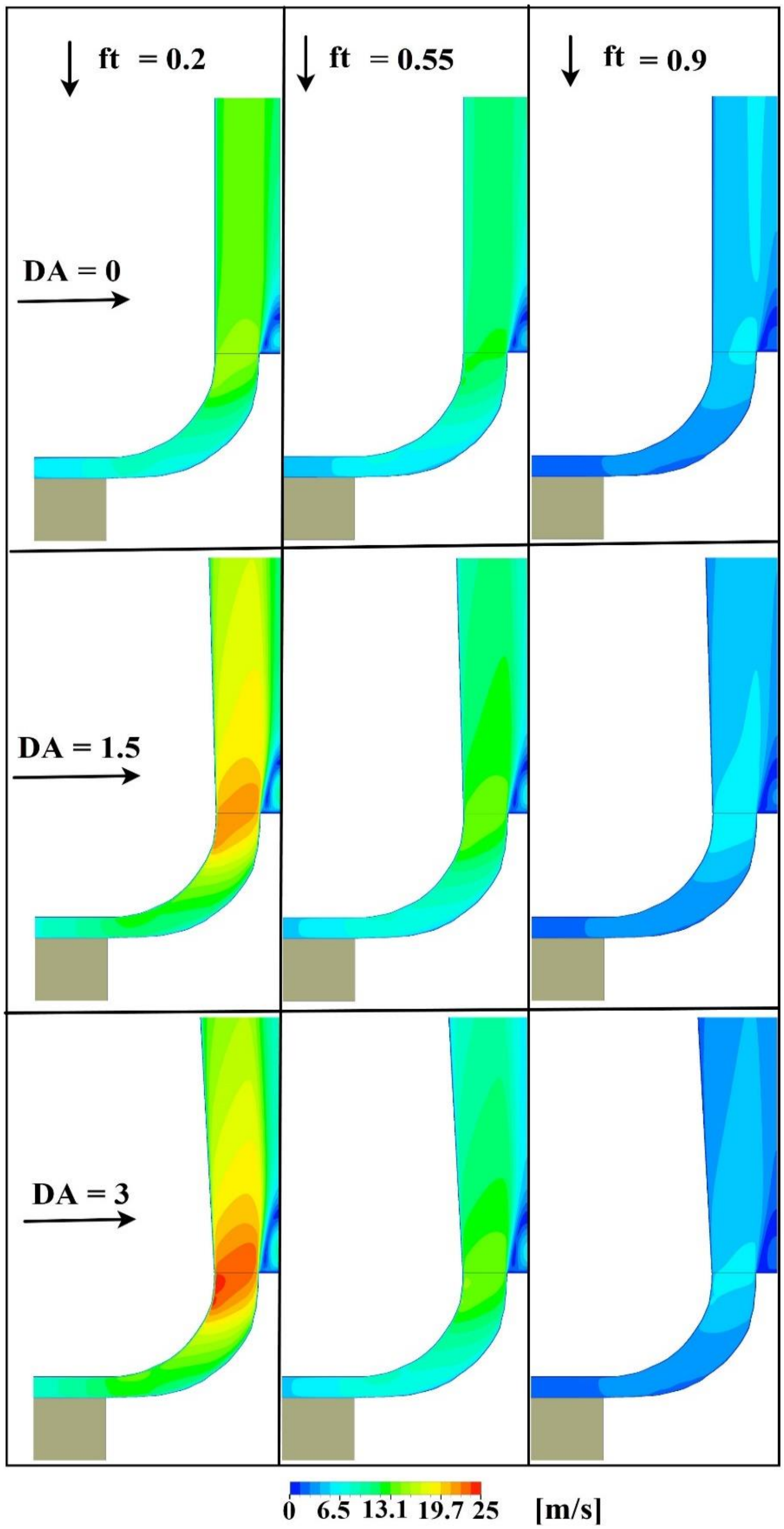

Fig. 6 Air velocity contour

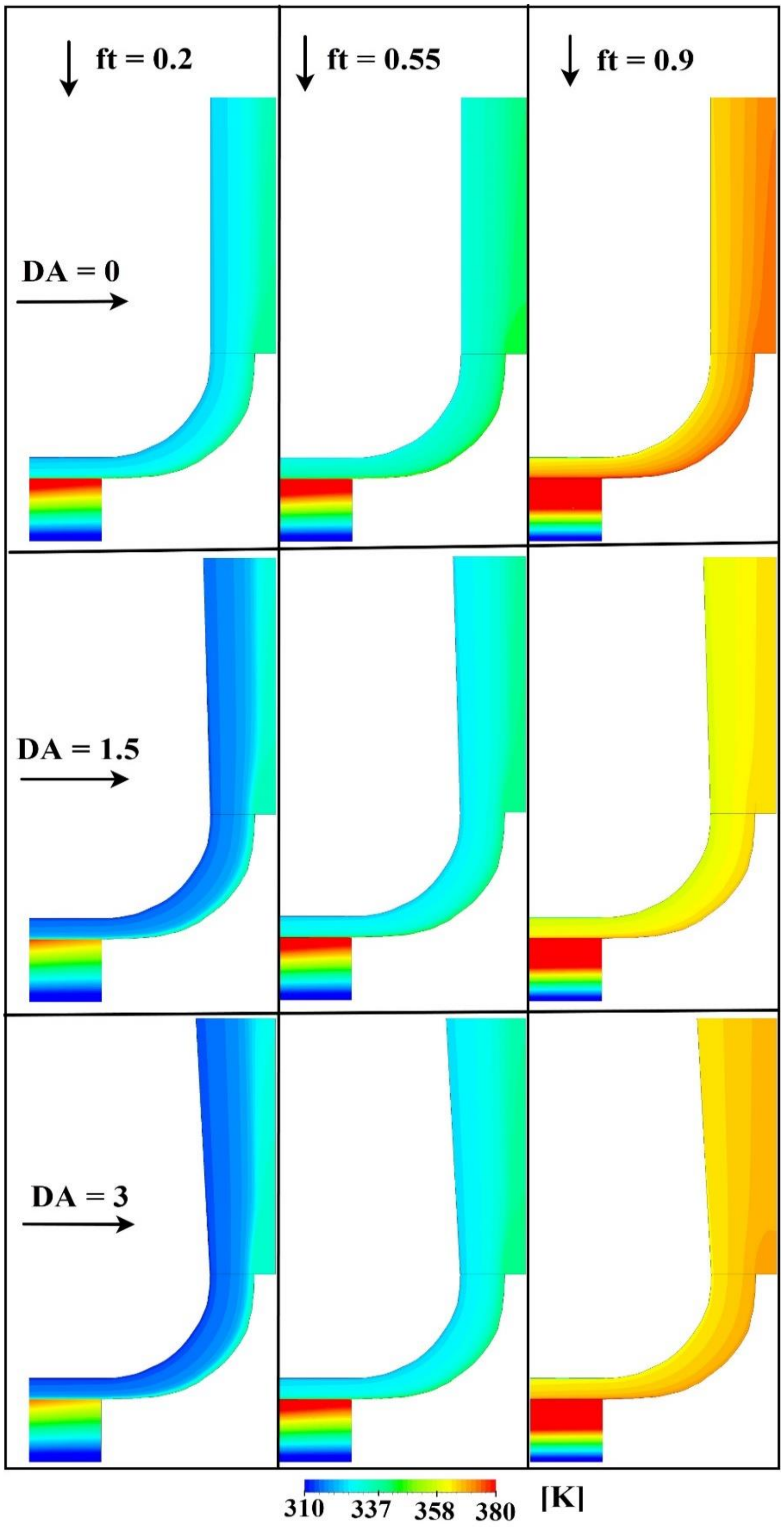

Fig. 7 Air temperature contour

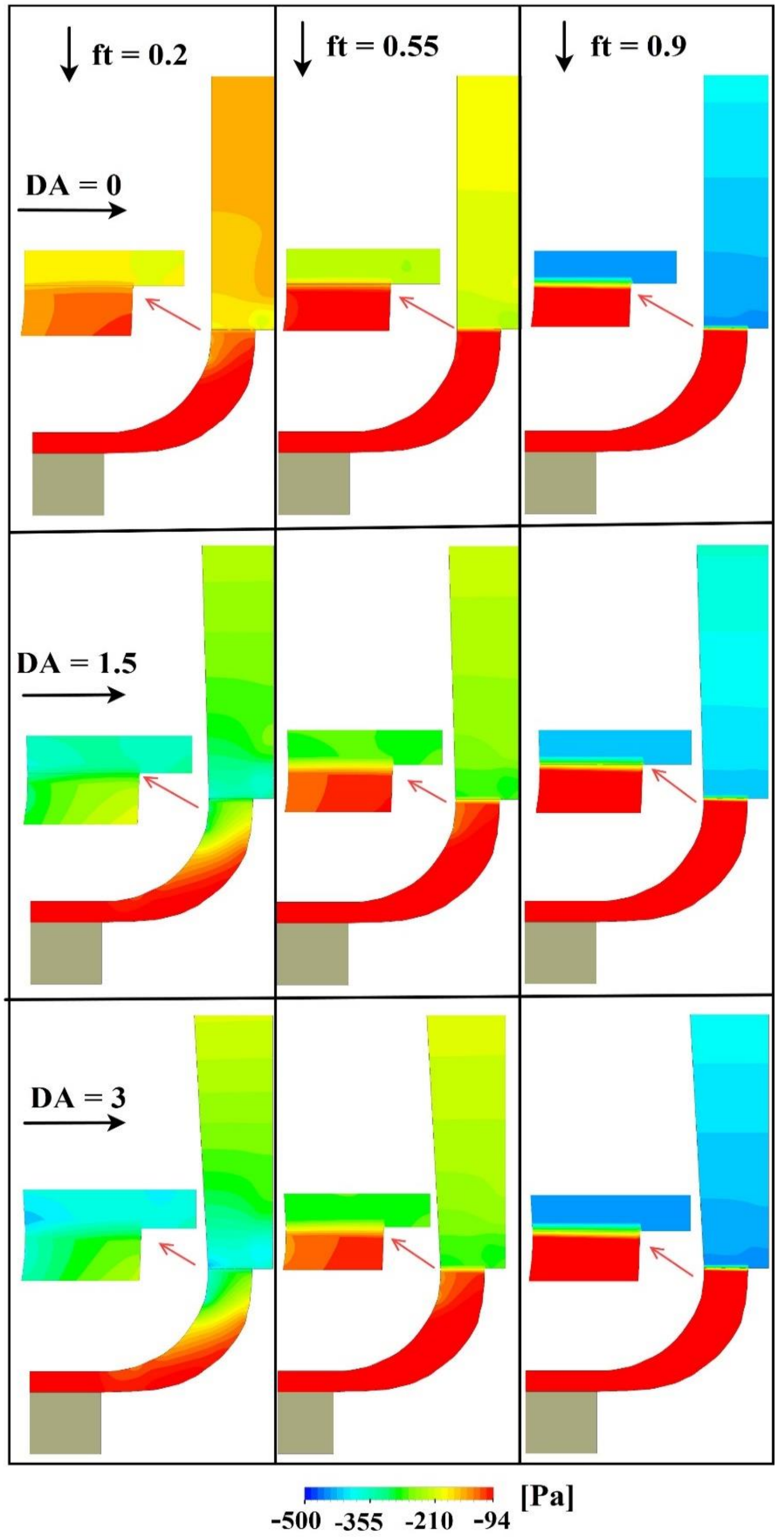

Fig. 8 Air static pressure contour

Fig. 9 (a) and (b) show the interaction effects of the ft and *DA* on the volume flow rate and temperature rise at the collector, respectively. The volume flow rate is continuously reduced by increasing ft because of the high amount of loss of kinetic energy in the turbine. Furthermore, the volume flow rate shows the ascending curve with increasing the *DA*, especially in the lower ft. This is attributed to the Δp_{total} enhancement that has the highest influence on the volume flow rate. With the rise of ft from 0.2 to 0.9, the volume flow rate is lessened from 2063 m^3/s to 435 m^3/s and from 1070 m^3/s to 418 m^3/s at *DA*=3° and *DA*=0°, respectively.

The temperature rise (ΔT) is increased with the increase of ft. Also, it is smoothly reduced by increasing *DA*. It can be concluded that ΔT is inversely related to the flow rate, which is consistent with Eq. (4). The lowest temperature rise is 16 K for *DA*=3°at ft = 0.2. On the other hand, the drawn diagram (Fig. 9 (b)) illustrates the highest temperature rise as 62 K for *DA*=3° at ft = 0.2.

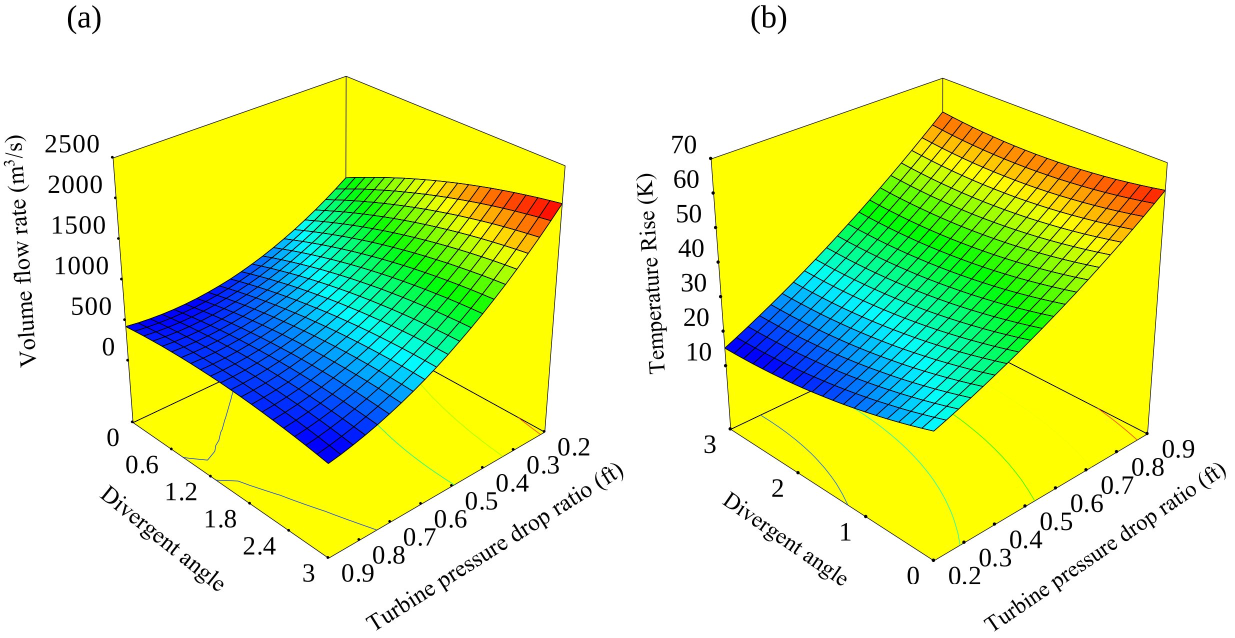
(a)

(b)

Fig. 9 Interaction effects of ft and *DA* on (a) the volume flow rate and (b) the temperature rise at the collector at *SR* = 800 W/m^2

The Δp_{total} in DSPP is the sum of two parameters, namely the buoyancy and pressure recovery. Fig. 10(a), (b), and (c) show the influence of the *DA* and ft on the buoyancy force, the pressure recovery, and the Δp_{total}, respectively. The buoyancy force is lessened as the *DA* increases due to the reduction of temperature differences. The buoyancy force drops from 210 Pa to 114 Pa for ft = 0.2 and from 447 to 426 for ft = 0.9.

On the other hand, pressure recovery is enhanced with increasing *DA*, which is more effective in the lower ft which is related to the outlet velocity reduction. The maximum pressure recovery with 467 Pa occurs for *DA*=3° at ft = 0.2 with the highest outlet velocity. Furthermore, since the chimney outlet-to-inlet area ratio is insignificant at *DA*=0, the minimum values of the pressure recovery become almost 5 Pa. Moreover, increasing ft results in the increment of the buoyancy force and the reduction of the pressure recovery.

According to Fig. 10(c), the Δp_{total} is increased with the rise of ft at the lower *DA*s related to the dominant buoyancy force. While at the higher *DA*, Δp_{total} has a different trend in a way that it decreases with increasing ft until it reaches a minimum value before starting to increase. In the descending part, pressure recovery has a higher effect than buoyancy, while vice-versa for the ascending part. By increasing *DA*, Δp_{total} enlarges from 216 Pa to 582 Pa at ft = 0.2 while it remains approximately constant as 447 Pa at ft = 0.9.

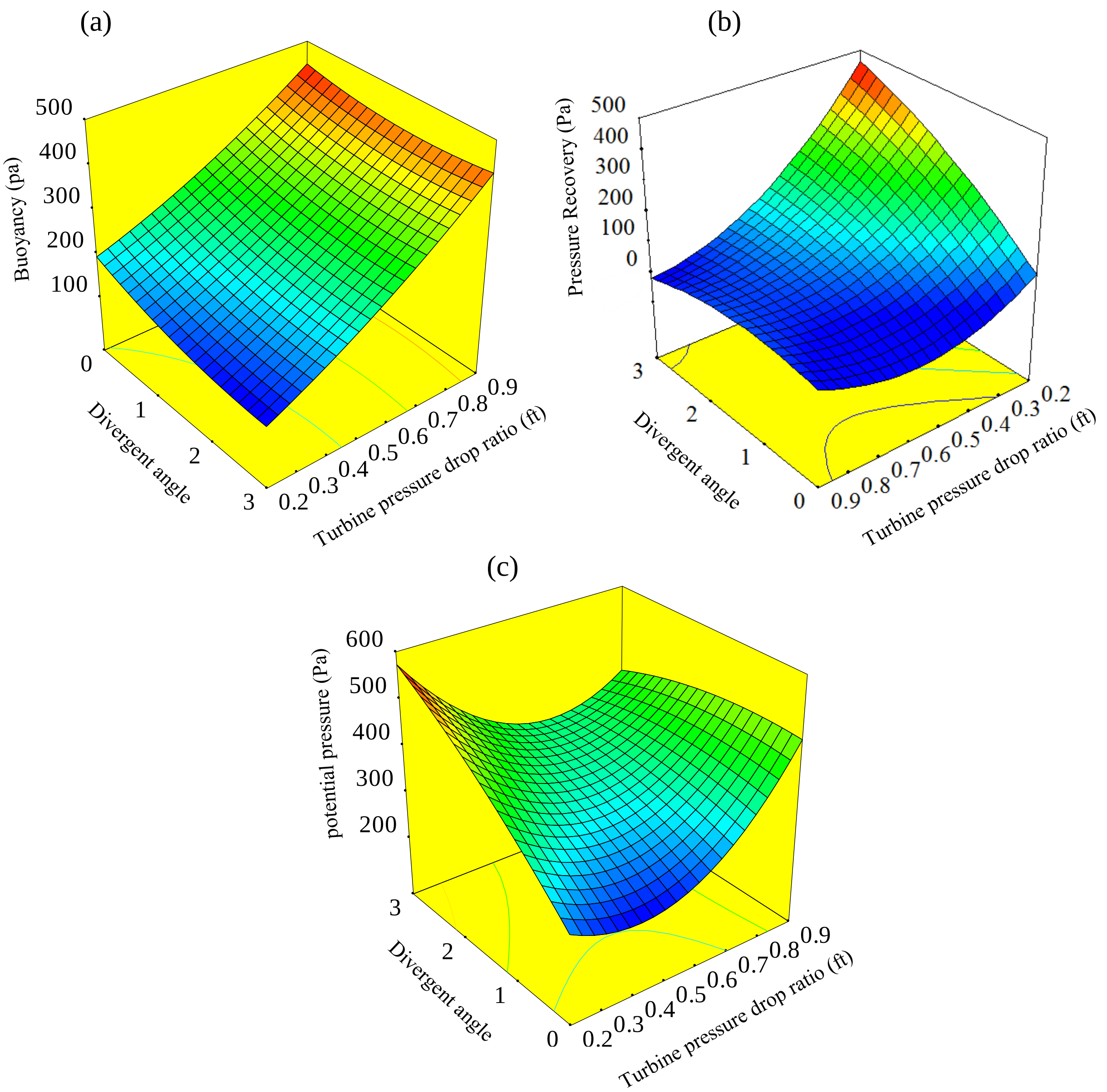

Fig. 10 Interaction effect of ft and *DA* on (a) buoyancy force and (b) pressure recovery, (c) total potential pressure at *SR* = 800 W/m^2

ft_{opt} and η_{max} are discussed in detail as follows. Firstly, in each *SR*, the efficiency was obtained at different *DA* and ft. Obviously, the ft_{opt} is achieved by maximizing the η as illustrated with a solid black line in Fig. 11(a) for *SR*=800 W/m^2. The value of η is increased by raising *DA* for all ft at the constant *SR* due to the increment of the volume flow rate, which is more noticeable at lower ft. Next, the RSM technique is applied to get the interaction effects between *DA* and *SR* on the ft_{opt} as plotted in Fig 11(b). The range of *SR* and *DA* are between 200 W/m^2 and 800 W/m^2 and 0° and 3°, respectively, which are covered in Fig. 11(b). The corresponding solid black line in Fig 11(a) is represented by curved black line in Fig. 11(b). The ft_{opt} is continuously reduced by increasing *DA*, which is steeper in the higher *SR*s, e.g., ft_{opt} is declined from 0.85 at an angle of 0 to 0.7 at an angle of 3 at *SR* = 200 W/m^2; however, it drops from 0.9 to 0.71 at *SR* = 800 W/m^2). The ft_{opt} is enhanced by increasing *SR* for all *DA*s; it is slightly influenced by the variations of *SR* at larger *DA*s. The ft_{opt} ranges from 0.85 at *SR* = 200 W/m^2 to approximately 0.9 at *SR* = 800 W/m^2 for *DA* at 0°, but this variation is lower at *DA* = 3°, which varies from 0.7 to 0.71. The results given in proposed model are in well agreement with the previous study for the *DA*=0° [26]. The following quadratic correlation is obtained by the RSM-CFD method for DSPP:

$$ft_{opt} = 0.85 + (5.33 \times 10^{-5} \times SR) - (0.12 \times DA) + (0.023 \times DA^2) \tag{19}$$

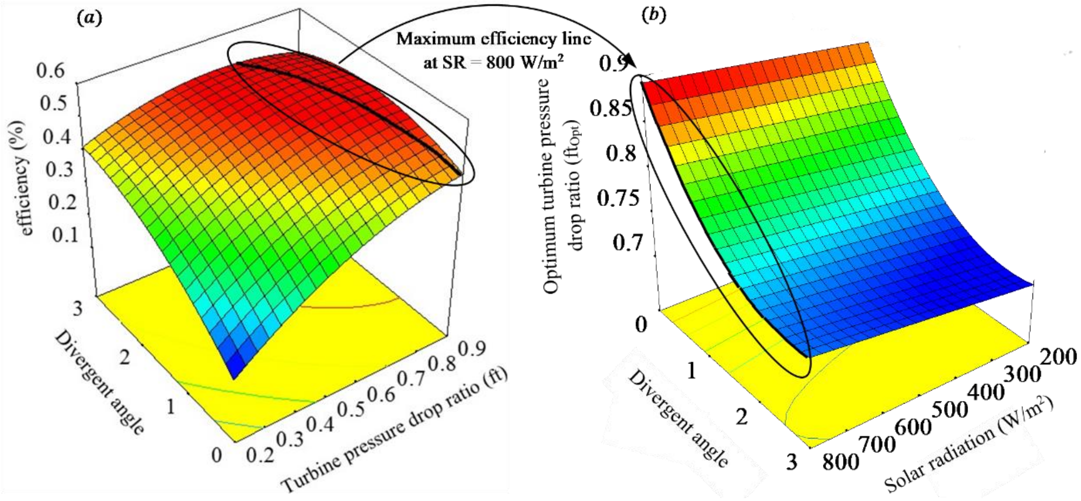

Fig. 11 (a) Interaction effect of the ft and *DA* on the η at *SR*=800 W/m2, (b) variation of the ft_{opt} with *DA* and *SR*

Finally, maximum efficiency (η_{max}) is obtained at the ft_{opt} for different *DA*s and *SR*s. As shown in Fig. 12, for all *DA*s, higher values of η_{max} is achieved by increasing the value of *SR*. This increment is more prominent in the lower *DA* such that in *DA*=0°, it varies from 0.42% at *SR* = 200 W/m^2 to 0.48% at *SR* = 800 W/m^2. However, the change for the same range of solar radiation at *DA* = 3° is from 0.47% to 0.50%. Also, the effect of *DA* on increasing η_{max} is higher at the lower *SR*s. As *DA* varies from 0° to 3°, η_{max} is increased around 0.06% and 0.04% at *SR* = 200 W/m^2 and *SR* = 800 W/m^2, respectively. The following relation is obtained for the η_{max} at the DSPP:

$$\eta_{max} = 0.42 + (9.57 \times 10^{-5} \times SR) + (0.03 \times DA) - (1.66 \times 10^{-6} \times DA \times SR) - (4.71 \times 10^{-8} \times SR^2) + (0.023 \times DA^2) \quad (20)$$

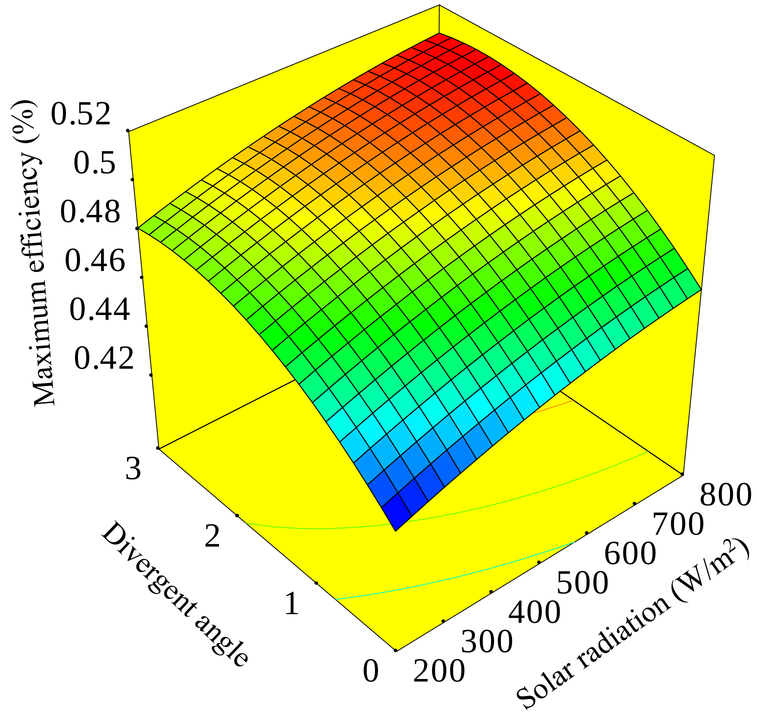

Fig. 12 Variation of the η_{max} with *DA* and *SR*

4. Conclusion

The main goal of the present article is to propose an RSM-CFD approach in order to investigate the ft_{opt} to reach the maximum efficiency of DSPP. For the first time, the DSPP performance under different *DA*s, fts, and *SR*s are evaluated through 2D axisymmetric numerical simulation and the RSM approach for the Manzanares prototype. The main findings are as follows:

1. Theoretical relationships indicate that the maximum power and the ft_{opt} for the CSPP is different from that of DSPP.

2. The volume flow rate in constant *SR* is enhanced by lowering the value of ft and increasing *DA*. The steeper curve of flow rate is achieved with respect to *DA* at the lower fts.

3. There is an inverse relationship between the effect of *DA* and ft on the temperature rise at the collector. Higher values of ft result in a more significant temperature rise, while higher values of *DA* result in lower temperature rise.

4. The behavior of pressure recovery is in contrast to the buoyancy force such that the higher values of the pressure recovery are achieved in higher *DA* values and lower ft.

5. The curve of total potential pressure (Δp_{total}) is ascending for lower *DA* while it is not the case in a high value of *DA*.

6. A quadratic correlation of ft_{opt} and η_{max} as a function of *SR* and *DA* is provided for the Manzanares prototype.

7. ft_{opt} varies in the range of 0.71 to 0.89. It is reduced by increasing the value of *DA* and lessening the *SR*.

8. The enhancement of η_{max} from lower *DA*s to higher *DA*s is more remarkable at lower *SR*s. It is 0.06% and 0.04% at *SR* = 200 W/m^2 and *SR* = 800 W/m^2, respectively. Furthermore, η_{max} is improved with the rise of *SR* at all *DA*s.

The calculated ft_{opt} at different *DA*s and *SR*s improve the efficiency of DSPP and is highly instrumental in the preliminary turbine design stages. Therefore, it is expected that the RSM-CFD method proposed here would be a pathway to predict the DSPP performance in different operating conditions.

Conflict of interest

No conflict of interest.

Funding: This research did not receive any specific grant from funding agencies in the public, commercial, or not-for-profit sectors.

References:

[1] Haaf W, Friedrich K, MAYR G, Schlaich J. Part I: Principle and Construction of the Pilot Plant in Manzanares. Int J Sol Energy 1983;2:3–20. https://doi.org/10.1080/01425918308909911.

[2] Khidhir DK, Atrooshi SA. Investigation of thermal concentration effect in a modified solar chimney. Sol Energy 2020;206:799–815. https://doi.org/10.1016/j.solener.2020.06.011.

[3] Aurybi MA, Gilani SI, Al-Kayiem HH, Ismaeel AA. Mathematical evaluation of solar chimney power plant collector, integrated with external heat source for non-interrupted power generation. Sustain Energy Technol Assessments 2018;30:59–67. https://doi.org/10.1016/j.seta.2018.06.012.

[4] Schlaich J. The Solar Chimney: Electricity from the Sun - Jörg Schlaich - Google Books. 1995.

[5] Cuce E, Sen H, Cuce PM. Numerical performance modelling of solar chimney power plants: Influence of chimney height for a pilot plant in Manzanares, Spain. Sustain Energy Technol Assessments 2020;39. https://doi.org/10.1016/j.seta.2020.100704.

[6] Zhou X, Wang F, Ochieng RM. A review of solar chimney power technology. Renew Sustain Energy Rev 2010;14:2315–38. https://doi.org/10.1016/j.rser.2010.04.018.

[7] Fallah SH, Valipour MS. Evaluation of solar chimney power plant performance: The effect of artificial roughness of collector. Sol Energy 2019;188:175–84. https://doi.org/10.1016/j.solener.2019.05.065.

[8] Mehdipour R, Baniamerian Z, Golzardi S, Murshed SMS. Geometry modification of solar collector to improve performance of solar chimneys. Renew Energy 2020;162:160–70. https://doi.org/10.1016/j.renene.2020.07.151.

[9] Von Backström TW, Gannon AJ. Compressible flow through solar power plant chimneys. J Sol Energy Eng Trans ASME 2000;122:138–45. https://doi.org/10.1115/1.1313528.

[10] Singh AP, Kumar A, Akshayveer, Singh OP. A novel concept of integrating bell-mouth inlet in converging-diverging solar chimney power plant. Renew Energy 2021;169:318–34. https://doi.org/10.1016/j.renene.2020.12.120.

[11] Lal S, Kaushik SC, Hans R. Experimental investigation and CFD simulation studies of a laboratory scale solar chimney for power generation. Sustain Energy Technol Assessments 2016;13:13–22. https://doi.org/10.1016/j.seta.2015.11.005.
[12] Koonsrisuk A, Chitsomboon T. Effects of flow area changes on the potential of solar chimney power plants. Energy 2013;51:400–6. https://doi.org/10.1016/j.energy.2012.12.051.
[13] Patel SK, Prasad D, Ahmed MR. Computational studies on the effect of geometric parameters on the performance of a solar chimney power plant. Energy Convers Manag 2014;77:424–31. https://doi.org/10.1016/j.enconman.2013.09.056.
[14] Ohya Y, Wataka M, Watanabe K, Uchida T. Laboratory experiment and numerical analysis of a new type of solar tower efficiently generating a thermal updraft. Energies 2016;9. https://doi.org/10.3390/en9121077.
[15] Hu S, Leung DYC, Chan JCY. Impact of the geometry of divergent chimneys on the power output of a solar chimney power plant. Energy 2017;120:1–11. https://doi.org/10.1016/j.energy.2016.12.098.
[16] Xu Y, Zhou X. Performance of divergent-chimney solar power plants. Sol Energy 2018;170:379–87. https://doi.org/10.1016/j.solener.2018.05.068.
[17] Kebabsa H, Said Lounici M, Daimallah A. Numerical investigation of a novel tower solar chimney concept. Energy 2021;214. https://doi.org/10.1016/j.energy.2020.119048.
[18] Cottam PJ, Duffour P, Lindstrand P, Fromme P. Solar chimney power plants – Dimension matching for optimum performance. Energy Convers Manag 2019;194:112–23. https://doi.org/10.1016/j.enconman.2019.04.074.
[19] Pradhan S, Chakraborty R, Mandal DK, Barman A, Bose P. Design and performance analysis of solar chimney power plant (SCPP): A review. Sustain Energy Technol Assessments 2021;47. https://doi.org/10.1016/j.seta.2021.101411.
[20] Haaf W. Part II: Preliminary Test Results from the Manzanares Pilot Plant. Int J Sol Energy 1984;2:141–61. https://doi.org/10.1080/01425918408909921.
[21] von Backström TW, Fluri TP. Maximum fluid power condition in solar chimney power plants - An analytical approach. Sol Energy 2006;80:1417–23. https://doi.org/10.1016/j.solener.2006.04.001.
[22] Nizetic S, Klarin B. A simplified analytical approach for evaluation of the optimal ratio of pressure drop across the turbine in solar chimney power plants. Appl Energy 2010;87:587–91. https://doi.org/10.1016/j.apenergy.2009.05.019.
[23] Xu G, Ming T, Pan Y, Meng F, Zhou C. Numerical analysis on the performance of solar chimney power plant system. Energy Convers Manag 2011;52:876–83. https://doi.org/10.1016/j.enconman.2010.08.014.
[24] Aligholami M, Sh. Khosroshahi S, R. Khosroshahi A. Hydrodynamic and thermodynamic enhancement of a solar chimney power plant. Sol Energy 2019;191:180–92. https://doi.org/10.1016/j.solener.2019.08.060.
[25] Li J, Guo H, Cheng Q, Huang S. Optimal turbine pressure drop for solar chimney-aided dry cooling system in coal-fired power plants. Energy Convers Manag 2017;133:87–96. https://doi.org/10.1016/j.enconman.2016.11.063.
[26] Guo P, Li J, Wang Y, Liu Y. Numerical analysis of the optimal turbine pressure drop ratio in a solar chimney power plant. Sol Energy 2013;98:42–8.

https://doi.org/10.1016/j.solener.2013.03.030.

[27] Guo P, Li J, Wang Y, Wang Y. Numerical study on the performance of a solar chimney power plant. Energy Convers Manag 2015;105:197–205. https://doi.org/10.1016/j.enconman.2015.07.072.

[28] Guo P, Li J, Wang Y, Wang Y. Evaluation of the optimal turbine pressure drop ratio for a solar chimney power plant. Energy Convers Manag 2016;108:14–22. https://doi.org/10.1016/j.enconman.2015.10.076.

[29] Zuo L, Dai P, Yan Z, Li C, Zheng Y, Ge Y. Design and optimization of turbine for solar chimney power plant based on lifting design method of axial-flow hydraulic turbine impeller. Renew Energy 2021;171:799–811. https://doi.org/10.1016/j.renene.2021.02.121.

[30] Sedighi AA, Deldoost Z, Karambasti BM. Effect of thermal energy storage layer porosity on performance of solar chimney power plant considering turbine pressure drop. Energy 2020;194. https://doi.org/10.1016/j.energy.2019.116859.

[31] Mehrpooya M, Shahsavan M, Sharifzadeh MMM. Modeling, energy and exergy analysis of solar chimney power plant-Tehran climate data case study. Energy 2016;115:257–73. https://doi.org/10.1016/j.energy.2016.09.006.

[32] Sangi R, Amidpour M, Hosseinizadeh B. Modeling and numerical simulation of solar chimney power plants. Sol Energy 2011;85:829–38. https://doi.org/10.1016/j.solener.2011.01.011.

[33] Abdi R, Rezazadeh N, Abdi M. Investigation of passive oscillations of flexible splitter plates attached to a circular cylinder. J Fluids Struct 2019;84:302–17. https://doi.org/10.1016/j.jfluidstructs.2018.11.001.

[34] Hassan A, Ali M, Waqas A. Numerical investigation on performance of solar chimney power plant by varying collector slope and chimney diverging angle. Energy 2018;142:411–25. https://doi.org/10.1016/j.energy.2017.10.047.

[35] Pastohr H, Kornadt O, Gürlebeck K. Numerical and analytical calculations of the temperature and flow field in the upwind power plant. Int J Energy Res 2004;28:495–510. https://doi.org/10.1002/er.978.

[36] Asfaram A, Ghaedi M, Agarwal S, Tyagi I, Gupta VK. Removal of basic dye Auramine-O by ZnS:Cu nanoparticles loaded on activated carbon: Optimization of parameters using response surface methodology with central composite design. RSC Adv 2015;5:18438–50. https://doi.org/10.1039/c4ra15637d.

[37] Subasi A, Sahin B, Kaymaz I. Multi-objective optimization of a honeycomb heat sink using Response Surface Method. Int J Heat Mass Transf 2016;101:295–302. https://doi.org/10.1016/j.ijheatmasstransfer.2016.05.012.